Materials Advances

ROYAL SOCIETY OF CHEMISTRY

PAPER

View Article Online
View Journal | View Issue

Check for updates

Cite this: *Mater. Adv.*, 2026, 7, 1188

Bio-based surface treatments for concrete durability: exploring the corrosion-inhibiting properties of *Costus afer* and *Chrysophyllum albidum* leaf extracts on fungal growth

Uzoma Charles Chukwuma, *[a] Joan Ijeoma Arimanwa,[ab] Kanayo Lucy Oguzie,[ac] Ugochi Nneka Kemka,[a] Ini-Ibehe Nabuk Etim,[ad] Sikandar Khan,[de] Kingsley O. Ukaegbu [f] and Emeka Emmanuel Oguzie[a]

Concrete structures are vulnerable to deterioration caused by microbial colonization and the corrosion of embedded steel reinforcements. Although conventional synthetic coatings and chemical inhibitors can be effective, they raise environmental and economic concerns. This study explores the use of ethanol extracts from *Costus afer* and *Chrysophyllum albidum* leaves as eco-friendly, dual-function additives for concrete protection. Phytochemical properties were analyzed using GC–MS and FTIR, while antifungal efficacy was assessed *via* the agar well diffusion method against fungal strains isolated from deteriorated concrete surfaces. Corrosion inhibition in simulated concrete pore solution [saturated $Ca(OH)_2$] was evaluated using potentiodynamic polarization (PDP), electrochemical impedance spectroscopy (EIS), and atomic force microscopy (AFM). In addition, geospatial techniques were applied to assess regional susceptibility to fungal biodeterioration. Landsat 8-derived normalized difference moisture index (NDMI) and land use/land cover (LULC) mapping assessments were conducted for Port Harcourt and Owerri to evaluate environmental drivers of microbial risk. Results showed that *C. albidum* exhibited superior antifungal activity across all isolates, with inhibition efficiencies of up to 99.8%. Surface analysis confirmed reduced roughness in treated samples. NDMI and LULC assessments revealed that vegetation moisture and impervious surface distribution strongly influence fungal colonization risk. This combined laboratory and remote sensing approach highlights the promise of *C. afer* and *C. albidum* extracts as sustainable, non-toxic additives for enhancing the durability of concrete structures, while emphasizing the need for region-specific environmental diagnostics in biodeterioration risk management.

Received 28th June 2025,
Accepted 17th November 2025

DOI: 10.1039/d5ma00687b

rsc.li/materials-advances

Open Access Article. Published on 20 November 2025. Downloaded on 6/21/2026 4:23:16 PM.
This article is licensed under a Creative Commons Attribution-NonCommercial 3.0 Unported Licence.

1. Introduction

Concrete structures are highly vulnerable to deterioration, especially in humid and nutrient-rich environments. Two major degradation pathways, microbial biodeterioration and corrosion of embedded steel reinforcements, pose serious threats to their durability and structural integrity.[1–4] These mechanisms weaken the concrete matrix, resulting in high maintenance costs and potential safety hazards.

Fungal colonization is one of the leading causes of concrete biodeterioration. Species such as *Aspergillus niger*, *Penicillium chrysogenum*, and *Cladosporium cladosporioides* thrive in moist environments, forming biofilms and secreting organic acids and enzymes that degrade the cement matrix.[5–7] These biological processes cause physical damage and discoloration and can also pose health risks through the release of airborne spores.[8] Previous studies have shown that fungal metabolites dissolve cement-binding agents, accelerating degradation. Bhattacharyya *et al.*[4] reported that *Aspergillus tamarii* was the most aggressive biodeteriorative species after three months of exposure, while *Fusarium* sp. had the least effect. Similarly, Chaudhuri *et al.* (2020)[9] observed severe degradation caused by

[a] *Africa Centre of Excellence in Future Energies and Electrochemical Systems (ACEFUELS), Federal University of Technology Owerri, P M B 1526 Owerri, Imo State, Nigeria. E-mail: chukwuma.uzoma20@gmail.com*
[b] *Department of Civil Engineering, Federal University of Technology Owerri, P M B 1526 Owerri, Imo State, Nigeria*
[c] *Department of Environmental Management, Federal University of Technology, P M B 1526 Owerri, Imo State, Nigeria*
[d] *Key Laboratory of Advanced Marine Materials, Key Laboratory of Marine Environmental Corrosion and Bio-fouling, Institute of Oceanology, Chinese Academy of Sciences, Qingdao 266071, P. R. China*
[e] *Department of Biotechnology, Shaheed Benazir Bhutto University, Sheringal 18000, KP, Pakistan*
[f] *Renaissance Africa Energy Company Limited, Port Harcourt, Rivers State, Nigeria*

© 2026 The Author(s). Published by the Royal Society of Chemistry

Open Access Article. Published on 20 November 2025. Downloaded on 6/21/2026 4:23:16 PM. This article is licensed under a Creative Commons Attribution-NonCommercial 3.0 Unported Licence.

A. tamarii over 180 days, and George *et al.*[6] documented major deterioration after 12 months of exposure to *Fusarium* sp. The acidic byproducts of fungal metabolism significantly increase the material's susceptibility to environmental attack.[8] To complement laboratory and field studies, remote sensing tools such as the normalized difference moisture index (NDMI) and land use/land cover (LULC) mapping can help assess fungal risk by identifying areas with high surface moisture and vegetation that promote microbial proliferation.

Corrosion of reinforcing steel in concrete is another major deterioration process. It occurs primarily in the presence of water, oxygen, and aggressive ions such as chlorides, which destroy the protective passive oxide layer on steel and initiate pitting corrosion.[10,11] Sliem *et al.*[12] reported that chloride ions accelerate corrosion by disrupting this passive layer. Additionally, carbonation lowers the pH of the concrete, further promoting corrosion and structural failure. To study these mechanisms, simulated concrete pore solution (SCPS) methods are commonly used for accelerated corrosion testing. SCPS usually contains saturated $Ca(OH)_2$[13,14] or cement extract solution.[15,16] Many studies have examined the effects of chloride concentration and temperature on steel corrosion in SCPS. Adewumi *et al.*[17] showed that increasing chloride concentration (500–2000 mg L^{-1}) and temperature (25–55 °C) increased the corrosion current density of carbon steel in $Ca(OH)_2$–KOH–NaOH solutions. Liu *et al.*[18] found that corrosion potential (E_{corr}) varied with chloride ion concentration in saturated $Ca(OH)_2$, while Poursaee[19] observed chloride-induced pitting when chloride ions destabilized the passive film formed on steel in SCPS.

The combined effects of fungal biodeterioration and steel corrosion significantly reduce the service life of concrete structures, particularly in industrial and marine environments where both mechanisms coexist. Recent research has explored modified concrete systems incorporating nanoadditives and corrosion inhibitors to mitigate microbial and chloride-induced damage.[20,21] Conventional antifungal and corrosion-inhibiting agents, such as halogenated compounds, quaternary ammonium salts, and metal oxides, have shown effectiveness.[22] For example, Kong *et al.*[23] evaluated dodecyl dimethyl benzyl ammonium chloride (DDBAC), copper phthalocyanine, sodium bromide, sodium tungstate, and zinc oxide and found that copper phthalocyanine enhanced concrete strength and microbial resistance, whereas zinc oxide, sodium bromide, and DDBAC inhibited microbes but weakened the concrete matrix. Similarly, nitrites and amines have been widely used as corrosion inhibitors. However, most of these compounds are toxic and environmentally unsafe.[24] Recent advances in engineered surfaces like slippery liquid-infused porous surfaces (SLIPS) have demonstrated remarkable anti-contaminant and anticorrosion performance on metallic substrates such as magnesium alloys.[20,25] While being methodologically distinct from the bio-based antifungal systems explored in this study, these technologies reflect a broader paradigm shift toward multifunctional surface protection. However, the reliance on synthetic components and high production costs associated with SLIPS has underscored the need for more sustainable, naturally derived alternatives.

Bio-concrete formulations that incorporate nano-modified fly ash or plant-based inhibitors have shown improved resistance to biodeterioration and corrosion, aligning with sustainable construction goals.[26] Plant-derived materials are particularly promising because they are rich in phytochemicals such as alkaloids, tannins, and flavonoids, which possess antimicrobial and corrosion-inhibiting properties. These compounds are typically non-toxic, biodegradable, and inexpensive to extract, making them viable candidates for eco-friendly corrosion and biodeterioration protection.

In this context, the present study investigates the dual-function performance of ethanol extracts from *Costus afer* and *Chrysophyllum albidum* leaves. The extracts are evaluated for their potential to inhibit fungal growth on concrete surfaces and to protect mild steel in simulated concrete pore environments. Using chemical characterization, microbiological assays, and electrochemical analyses, this work proposes a sustainable strategy to enhance the durability of reinforced concrete in aggressive environments.

2. Materials and methods

2.1 Preparation of plant extracts

Fresh leaves of *Costus afer* and *Chrysophyllum albidum* were sourced from a local market and authenticated at the Department of Crop Science Technology, Federal University of Technology, Owerri. Each batch (15 g) of dried, pulverized leaves was macerated in 300 mL of ethanol for 72 hours. The mixtures were filtered, and the filtrates were stored as ethanol extracts for subsequent analyses.

2.2 Fourier-transform infrared spectroscopy (FTIR) analysis

FTIR analysis was conducted to identify functional groups in powdered leaves and extracts using a PerkinElmer Spectrum 2 FTIR spectrometer. Spectra were recorded in the range of 4000–450 cm^{-1}.

2.3 Gas chromatography–mass spectrometry (GC–MS) analysis

Phytochemical profiling of the extracts was performed using a Shimadzu GC–MS-QP2010 PLUS system. Six microliters of extract, pre-sonicated with *n*-hexane, were injected. Compound identification was based on spectral comparison with the NIST Library.

2.4 Collection of concrete samples

Deteriorated concrete samples were collected from surfaces in Ozuoba, Port Harcourt, and FUTO, Owerri. Scrapings were stored in labeled sterile bags and transported for microbial analysis.

2.5 Preparation of the culture medium

Sabouraud dextrose agar (SDA) was prepared by dissolving 62 g of SDA powder in 1 L of distilled water and sterilizing it at 121 °C for 15 minutes.

Open Access Article. Published on 20 November 2025. Downloaded on 6/21/2026 4:23:16 PM. This article is licensed under a Creative Commons Attribution-NonCommercial 3.0 Unported Licence.

2.6 Fungal isolation and identification

Concrete samples (10 g) were vortexed with 90 mL of sterile saline for 3 min and then serially diluted to 10^{-4}. Aliquots (0.1 mL) were plated on SDA and incubated (26 °C, 5 d). The fungal isolates were observed morphologically and then examined microscopically after staining with lactophenol cotton blue (10× and 40× magnification).

2.7 Antifungal susceptibility testing

Using the agar well diffusion method, fungal cultures (standardized to 0.5 McFarland) were mixed with molten SDA (45 °C) and poured into plates. Wells (6 mm diameter) were loaded with 100 μL test extracts at varying concentrations. After refrigeration (30 min) and incubation (26 °C, 24–48 h), inhibition zones were measured against sterile water controls.

2.8 Preparation of mild steel coupons

A36 mild steel coupons (1.0 × 1.0 × 0.2 cm) with composition have been reported elsewhere (Onuoha *et al.* 2024). They were embedded in PTFE with 1 cm^2 exposed. Surfaces were sequentially abraded (800 → 1200 grit), degreased (ethanol → acetone), and desiccated before use.

2.9 Preparation of the simulated concrete pore solution (SCPS)

The SCPS was prepared by dissolving 2 g of $Ca(OH)_2$ in 1 L of distilled water, yielding a pH of 12.5 at 36.5 °C.

2.10 Electrochemical measurements

Electrochemical testing was carried out using a Corrtest potentiostat/galvanostat. A three-electrode cell setup included mild steel as the working electrode, platinum as the counter electrode, and a saturated calomel electrode as the reference electrode. PDP scans were recorded from −0.25 V to +0.25 V at 0.2 mV s^{-1}. EIS was performed using a 5 mV AC signal from 100 kHz to 10 MHz.

2.11 Atomic force microscopy (AFM) analysis

Steel surfaces after 72 h of immersion in $Ca(OH)_2$ solution with/without extracts were examined using an nGauge AFM system. Surface roughness parameters (S_q and S_a) were recorded.

2.12 Remote sensing

This study applied geospatial analysis techniques to support the evaluation of environmental conditions potentially influencing fungal deterioration of concrete infrastructure in two Nigerian urban centres: Port Harcourt and Owerri.

2.12.1 Satellite imagery acquisition and preprocessing. Landsat 8 Operational Land Imager (OLI) data from the year 2025 were acquired *via* the USGS Earth Explorer platform. All imagery was subjected to atmospheric correction and radiometric calibration to ensure spectral consistency. Processing and analysis were conducted using ArcGIS Desktop 10.x.

2.12.2 Normalized difference moisture index (NDMI) mapping. The normalized difference moisture index (NDMI) was calculated to assess vegetation moisture levels across the study areas using eqn (1):

$$\mathrm{NDMI} = \frac{(\mathrm{NIR} - \mathrm{SWIR})}{(\mathrm{NIR} + \mathrm{SWIR})} \quad (1)$$

where NIR and SWIR correspond to the near-infrared and shortwave infrared bands of the Landsat imagery, respectively. NDMI raster layers were generated in ArcGIS and classified to represent gradients in vegetation moisture, ranging from low to high. These maps were used to visualize spatial patterns in environmental moisture conditions surrounding built-up areas.

2.12.3 Land use/land cover (LULC) classification. Supervised classification was performed on the Landsat 8 imagery to produce land use/land cover (LULC) maps for both cities. The classification scheme included the following classes: bare surface, forest vegetation, farm vegetation, paved surface, water body, cloud cover, and shadow. Training samples were collected from known ground features, and classification accuracy was validated using ground-truth data and confusion matrix analysis. The areal extent of each land cover type was computed to support environmental characterization.

2.12.4 Spatial data extraction and zonal analysis. Zonal statistics were performed to extract average NDMI values for each city's urban boundary polygon. This enabled spatial quantification of vegetation moisture within defined municipal extents. Similarly, the proportional distribution of LULC categories within each city boundary was derived to assess the composition of land surface types, particularly impervious surfaces that may be prone to fungal colonization.

3. Results and discussion

3.1 GC–MS analysis

The phytochemical components present in ethanol extracts of both *C. afer* and *C. albidum* were identified using gas chromatography–mass spectrometry (GC–MS). The obtained chromatograms are illustrated in Fig. 1, with detailed peak assignments given in Table S1 (SI).

The GC–MS analysis revealed twenty phytochemical constituents in both *Costus afer* and *Chrysophyllum albidum* ethanol extracts (Table 3). Several of these compounds have been reported in the literature for their antifungal and corrosion-inhibiting activities.

In *C. afer*, eight major bioactive compounds were identified. Neophytadiene (peaks 1 and 3), a diterpenoid known for its antifungal and antimicrobial activity, has been previously reported in various plant extracts.[27,28] Squalene (peak 8), a triterpene, acts as an inhibitor of squalene synthase, interfering with ergosterol biosynthesis in fungal membranes.[29,30] Methyltetracosane (peak 11) is a long-chain hydrocarbon frequently associated with bioactive plant fractions. Compounds such as α-tocospiro B and α-tocospiro O (peaks 12 and 13), structural analogues of α-tocopherol, demonstrate antioxidant and antimicrobial activities.[31,32] Additional notable components

© 2026 The Author(s). Published by the Royal Society of Chemistry

Open Access Article. Published on 20 November 2025. Downloaded on 6/21/2026 4:23:16 PM.
This article is licensed under a Creative Commons Attribution-NonCommercial 3.0 Unported Licence.

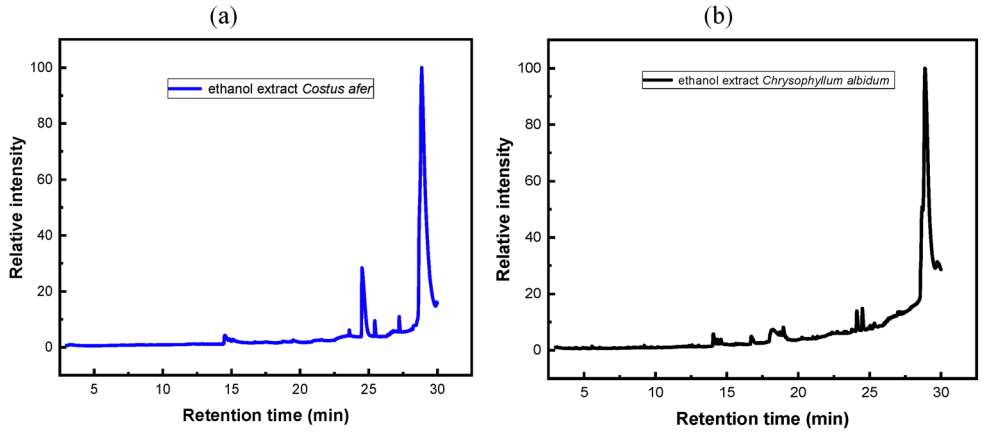

Fig. 1 GC–MS chromatogram of ethanol extracts of (a) *C. afer* and (b) *C. albidum*.

include ethyl iso-allocholate (peak 16), larossic acid acetate (3β) (peak 20), and (*R*)-6*b*,8*a*-epoxy-1,4,4*a*,5,6,7,8,8*a*-octamethyl-decahydro derivatives (peak 18), all of which have been reported in antifungal or bioactive plant materials.

Similarly, the *C. albidum* extract contained twelve antifungal constituents. Squalene (peaks 10 and 12) was again identified as a dominant bioactive compound. Siloxane derivatives such as cyclononasiloxane, octadecamethyl- (peak 6) and cyclotetrasiloxane, hexadecamethyl- (peak 8) exhibit known antimicrobial characteristics. Fatty acid esters, hexadecanoic acid, ethyl ester (peak 5) and octadecenoic acid, ethyl ester (peak 7) act by disrupting fungal membrane integrity.[33,34] Other notable constituents include eicosane (peak 1), neophytadiene (peak 2), and 3,7,11,15-tetramethyl-2-hexadecen-1-ol (peaks 3, 4), structurally similar to antifungal phytol derivatives.[28,35] Triterpenoids such as lup-20(29)-en-3-ol, acetate (peak 17), 7,8-epoxylanostan-11-ol-3-one (peak 18), and 9,19-cyclolanostan-3-ol, acetate (peak 20) further support antifungal potential.

Both extracts possess multiple phytochemicals with molecular features typical of effective organic corrosion inhibitors, aromatic rings, conjugated double bonds, and heteroatoms (N, S, and O). These structural motifs enhance adsorption on metal surfaces, thereby reducing corrosion rates.[36,37] Compared with reported plant-based inhibitors such as *Gongronema latifolium* and *Ocimum gratissimum*, *C. afer* and *C. albidum* demonstrate broader multifunctionality and potential synergistic protection.[38,39]

3.2 Corrosion studies

3.2.1 Potentiodynamic polarization. Potentiodynamic polarisation experiments were carried out to assess the effects of the extracts on the cathodic and anodic corrosion reactions. Fig. 2 shows the effect of *C. afer* on the polarisation behaviour of mild steel in $Ca(OH)_2$, while Fig. 3 shows the effect of *C. albidum*. The corresponding polarisation parameters are given in Table 1. The results show that mild steel underwent active dissolution in $Ca(OH)_2$ without and with the extracts, with no distinctive transition towards passivation. The extracts influenced both the cathodic and the anodic reactions, implying

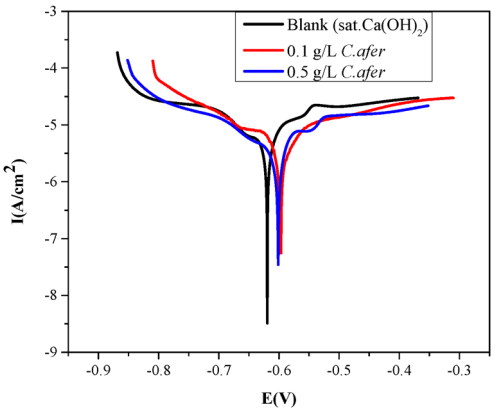

Fig. 2 Potentiodynamic polarization plots of mild steel exposed in saturated $Ca(OH)_2$ solution without and with different concentrations of *C. afer*.

that they functioned *via* a mixed-inhibition mechanism. *C. afer* can be seen to shift E_{corr} towards more positive (anodic) potentials, with more pronounced anodic polarisation effect, leading to significant reductions in the values of the corrosion

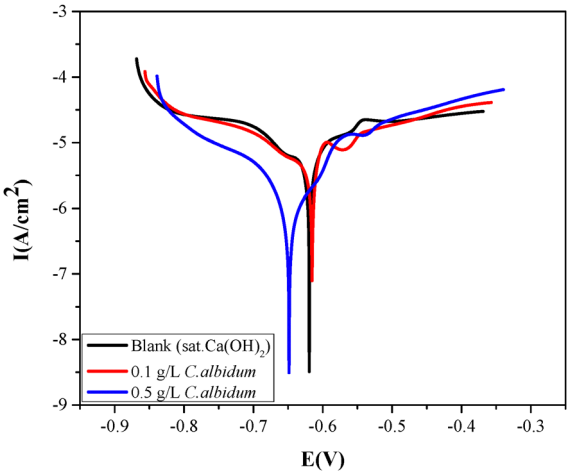

Fig. 3 Potentiodynamic polarization plots of mild steel exposed in saturated $Ca(OH)_2$ solution without and with different concentrations of *C. albidum*.

Open Access Article. Published on 20 November 2025. Downloaded on 6/21/2026 4:23:16 PM.
This article is licensed under a Creative Commons Attribution-NonCommercial 3.0 Unported Licence.

Table 1 PDP measurement results of mild steel in $Ca(OH)_2$ solution

System	Concentration (g L^{-1})	β_a (mV dec^{-1})	β_c (mV dec^{-1})	j_{corr} (μA cm^{-2})	E_{corr} (V)	IE (%)
Blank (sat. $Ca(OH)_2$)	—	274.3	509.3	1590.5	−0.619	—
C. afer	0.1	141.0	56.0	27.8	−0.597	98.25
	0.5	98.7	77.8	262.2	−0.601	83.51
C. albidum	0.1	101.5	163.8	459.2	−0.615	71.12
	0.5	179.6	188.1	3.20	−0.649	99.8

current density (j_{corr}). *C. albidum* also notably reduced i_{corr} and shifted E_{corr} towards more cathodic values, with more pronounced cathodic polarisation. The inhibition efficiency (IE) was calculated using eqn (2),[40,41] where $j_{corr,0}$ and j_{corr} represent the corrosion current densities in the absence and in the presence of the extracts.

$$IE = \frac{j_{corr,0} - j_{corr}}{j_{corr,0}} \times 100\% \quad (2)$$

The maximum inhibition efficiencies 98.25% (for *C. afer*) and 99.8% (for *C. albidum*) are remarkable and confirm the potential of both extracts as eco-friendly, green anticorrosion additives for mild steel in SCPS. These results are comparable to or better than natural inhibitors reported in the literature, such as ginger extract which achieved 91.2% efficiency.[42]

3.2.2 Electrochemical impedance spectroscopy (EIS). EIS was employed to evaluate the kinetics of the electrode reactions and the corrosion mechanisms occurring at the Fe/SCPS interface. This analysis provided insight into how the biomass extracts influenced these processes. The impedance responses of the Fe/SCPS system, in the absence and in the presence of *C. afer* and *C. albidum* extracts at concentrations of 0.1 g L^{-1} and 0.5 g L^{-1}, are presented in Fig. 4 and 5 in both Nyquist and Bode formats. The corresponding impedance parameters are summarised in Table 2.

The Nyquist plots display depressed capacitive semicircles characteristic of charge transfer processes, where the semicircle diameter represents the charge transfer resistance (R_{ct}) at the Fe/$Ca(OH)_2$ interface.[43] The observed depression in the semicircles is attributed to frequency dispersion effects caused by surface heterogeneity and roughness variations of the steel.[44] Due to this non-ideal frequency response, a

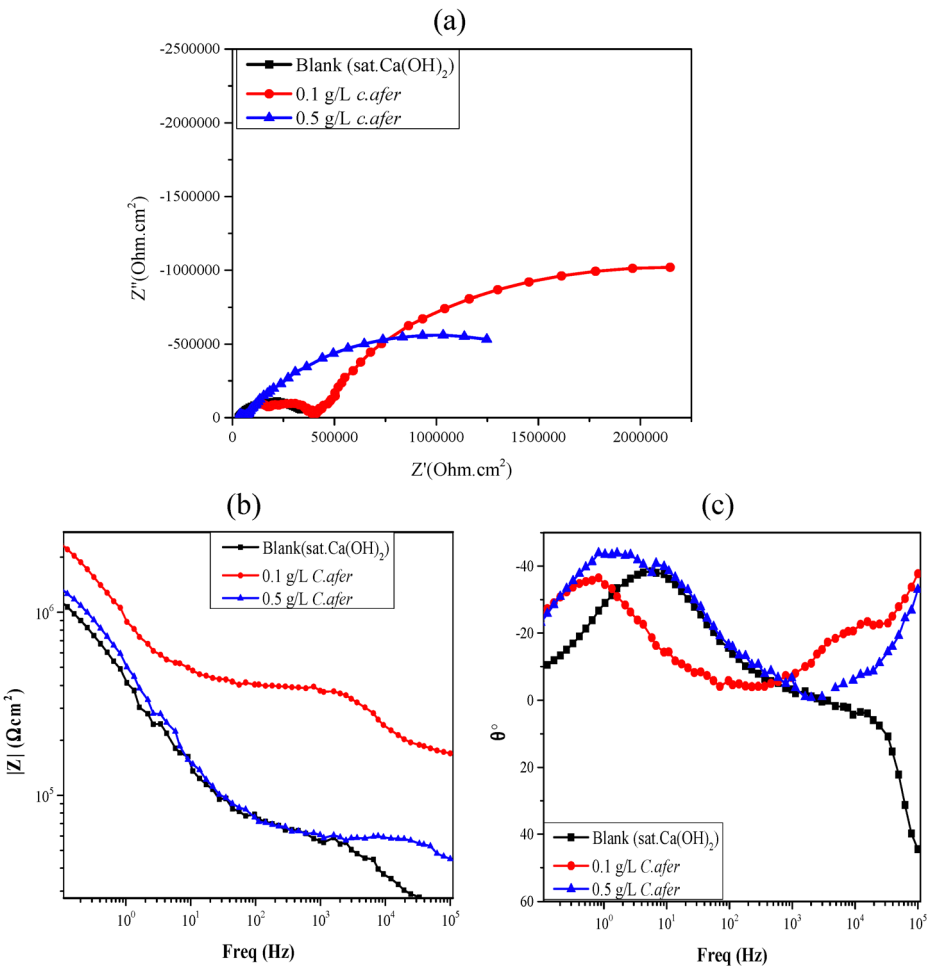

Fig. 4 (a) Nyquist, (b) Bode modulus, and (c) Bode phase angle plots of mild steel immersed in $Ca(OH)_2$ with different concentrations of *C. afer*.

© 2026 The Author(s). Published by the Royal Society of Chemistry

Open Access Article. Published on 20 November 2025. Downloaded on 6/21/2026 4:23:16 PM.
This article is licensed under a Creative Commons Attribution-NonCommercial 3.0 Unported Licence.

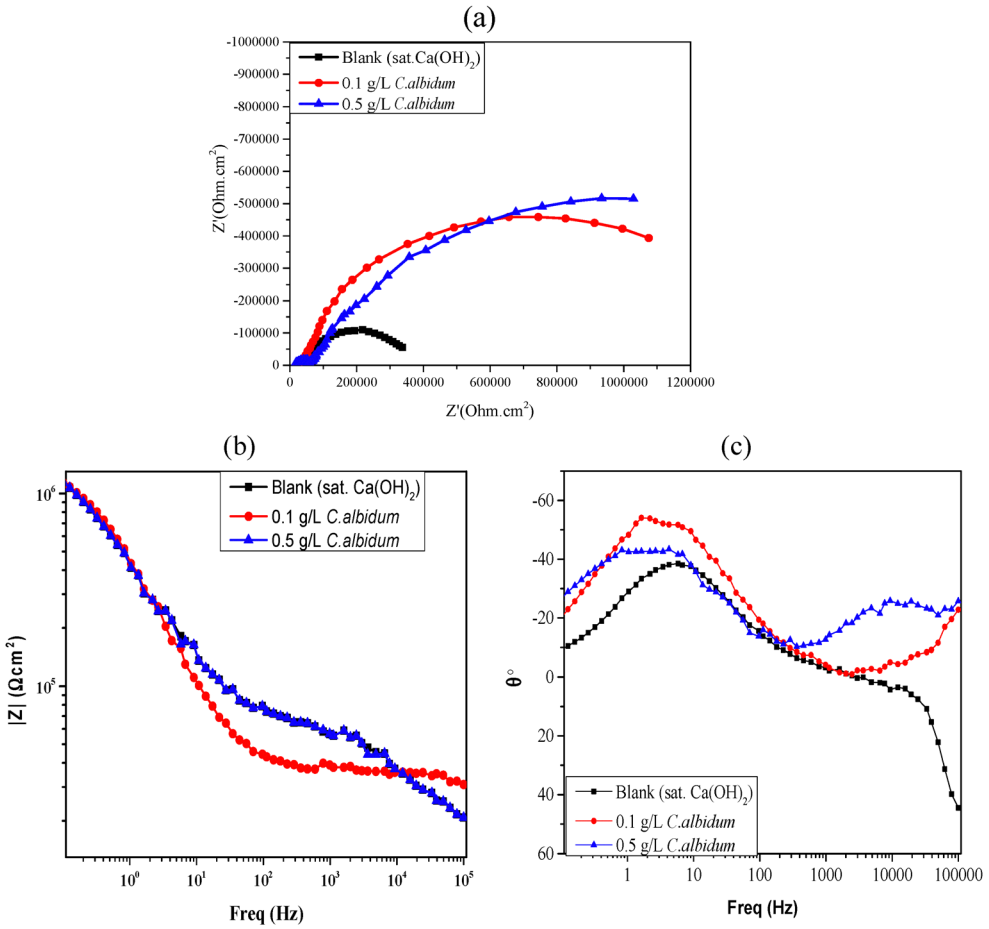

Fig. 5 (a) Nyquist, (b) Bode modulus, and (c) Bode phase angle plots of mild steel immersed in $Ca(OH)_2$ with different concentrations of *C. albidum*.

Table 2 Electrochemical impedance parameters for mild steel in $Ca(OH)_2$ without and with extracts

System	R_s (Ω cm^2)	R_{ct} (kΩ cm^2)	R_f (kΩ cm^2)	CPE (μF cm^{-2})	n	W (Ω s$^{-\frac{1}{2}}$)	C_{dl} (μF cm^{-2})	IE (%)
Blank (sat. $Ca(OH)_2$)	32.3	338.0	—	0.808	0.88	—	3.72	—
C. afer (0.1 g L^{-1})	397.0	3190.0	112.0	0.373	0.90	55.2	1.67	89.41
C. afer (0.5 g L^{-1})	59.3	1940.0	98.7	0.522	0.89	48.7	2.56	82.61
C. albidum (0.1 g L^{-1})	35.7	1360.0	86.5	0.487	0.91	52.4	1.74	75.25
C. albidum (0.5 g L^{-1})	58.0	1960.0	107.0	0.704	0.92	50.1	2.24	82.78

constant phase element (CPE) was introduced into the equivalent circuit model to account for deviations from ideal dielectric behavior.

Nyquist plots obtained from electrochemical impedance spectroscopy revealed marked differences between the uninhibited system and those treated with *Costus afer* and *Chrysophyllum albidum* extracts. In the untreated control sample simulated concrete pore solution (SCPS), a small, depressed semicircle was observed, characteristic of active corrosion with minimal surface protection. The corresponding charge transfer resistance (R_{ct}) was relatively low at 3.38×10^5 Ω cm^2, while the double-layer capacitance (C_{dl}) was high (3.72 μF cm^{-2}), reflecting a highly conductive interface. This behaviour is typically modelled using a simple Randles circuit [$R_s(Q_{dl}R_{ct})$], which is appropriate for systems with unimpeded electrochemical reactions. The depressed nature of the semicircle arcs is attributed to frequency dispersion, commonly arising from surface heterogeneity and microstructural roughness.[44]

The C_{dl} values were estimated from CPE parameters using the modified Brug formula:

$$C_{dl} = \text{CPE} \times (R_{ct})^{1-n} \quad (3)$$

Open Access Article. Published on 20 November 2025. Downloaded on 6/21/2026 4:23:16 PM. This article is licensed under a Creative Commons Attribution-NonCommercial 3.0 Unported Licence.

where n is the CPE exponent, indicative of surface uniformity. Higher n-values and lower C_{dl} values suggest the formation of more compact and homogeneous films.

Upon addition of the plant extracts, the diameter of the Nyquist semicircles increased significantly, indicating enhanced inhibition *via* formation of surface films that impede charge transfer. R_{ct} values increased by nearly an order of magnitude, up to $3.19 \times 10^6\ \Omega\ cm^2$ for *C. afer* and $1.96 \times 10^6\ \Omega\ cm^2$ for *C. albidum*, while C_{dl} values concurrently decreased to 1.67–2.24 $\mu F\ cm^{-2}$. This reduction in interfacial capacitance is consistent with increased double-layer thickness and lower dielectric constant at the interface, both attributable to adsorption of extract molecules. The impedance behavior of the inhibited systems is best described using an extended Randles circuit, $[R_s(Q_f(R_f(Q_{dl}R_{ct}))]$, incorporating film resistance (R_f) in series with R_{ct} and, in some cases, a Warburg element (W) to account for diffusional resistance through the adsorbed bioorganic layer. Interestingly, the Nyquist plots also exhibit a second, smaller high-frequency capacitive loop in the presence of both extracts. This feature is attributed to the presence of a discrete adsorbed film introducing an additional interfacial process, or potentially, the alteration of electrochemical reaction pathways, such as cathodic oxygen reduction or anodic iron dissolution, resulting in multiple time constants. These are further evident in the corresponding Bode phase plots. Overall, the evolution of the impedance response confirms that the extracts do not merely retard corrosion, but establish a protective barrier that effectively resists both charge transfer and mass transport at the steel/SCPS interface.

Corrosion inhibition efficiency (IE%) values shown in Table 2 were estimated by comparing the values of the charge transfer resistance in the absence ($R_{ct/Blk}$) and in the presence of the extracts ($R_{ct/Ext}$) as follows:

$$IE\% = \frac{R_{ct/Ext} - R_{ct/Blk}}{R_{ct/Ext}} \times 100\% \quad (4)$$

The inhibition efficiencies obtained from both polarization and impedance measurements confirm the high corrosion protection offered by the plant extracts. The slightly higher values from polarization studies (up to 99.8%) compared to impedance experiments (up to 89.4%) can be attributed to differences in measurement principles, with polarization experiments capturing the instantaneous suppression of corrosion reactions, and impedance spectroscopy reflecting the longer-term resistive and capacitive properties of the inhibitor film. The modest discrepancy suggests that while the extracts rapidly inhibit corrosion, the protective films may exhibit minor porosity or diffusion effects over extended exposure.

3.3 Fourier-transform infrared spectroscopy (FTIR) analysis

FTIR analysis was undertaken to confirm the adsorption of the extract organic matter on the Fe/$Ca(OH)_2$ interface. To achieve this, the dried leaf powders of *C. afer* and *C. albidum*, as well as the ethanol extracts and scrapings of the corrosion product layer on mild steel immersed in $Ca(OH)_2$ containing 0.5 g L^{-1} of *C. afer* and *C. albidum* extracts, were analyzed using FTIR (Fig. 6). The idea here was to identify the functional groups within plant leaves and extracts and to match these with any functional groups identified in the corrosion product layer.

The FTIR peak assignments are presented in Table 3. The FTIR spectrum for *C. afer* is shown in Fig. 6a, and the peak at 3338 cm^{-1} corresponds to the presence of alcohol (O–H). The peaks at 2974.20 and 2884.20 cm^{-1} indicate the presence of alkane (C–H). The peaks at 1380.39 cm^{-1} and 1328.32 cm^{-1} correspond to the presence of aldehydes (C–H bend) and sulfone, respectively. The peaks at 1087.68 cm^{-1} and 1045.58 cm^{-1} indicate the presence of functional groups such as amine (C–N stretching) and sulfoxide (S═O stretching), respectively. The peaks from 879.94 to 619.92 cm^{-1} reveal the presence of 1,3-disubstituted benzene (C–H bending) and halo compounds (C–Cl stretching). For *C. albidum* (Fig. 6b), peaks were recorded at 3339.01, 2974.43, 2884.62, 1654.23 and 1087.63, 1380.51, 1328.28, 879.87, and 611.43 cm^{-1} that correspond to O–H stretching (class: alcohol), C–H stretching (class: alkane), N–H stretching (class: amine salt), C–N stretching (class: imine/oxine, amine), C–H bending (class: aldehyde), S═O stretching (class: sulfone), C–H bending (class: 1,3-disubstituted benzene) and C–Cl stretching (class: halo compound), respectively. For both *C. afer* and *C. albidum*, characteristic peaks corresponding to O–H stretching (hydroxyl groups), C–N (amine groups), and C–H stretching (alkanes) were observed, indicating the presence of alkaloids, flavonoids, tannins and other bioactive compounds known for their antimicrobial and anticorrosion activities.[45]

FTIR spectra of the extracts and corrosion product layers from *C. afer* (Fig. 6a2) and *C. albidum* (Fig. 6b2) revealed bands corresponding to O–H (alcohols), C–N (amines), and S═O (sulfoxides) stretching and aromatic C–H bending. These functional groups are commonly involved in adsorption processes and metal surface complexation. Their presence in both the original extracts and the steel surface residue confirms the interaction between the extract constituents and the steel surface, forming a barrier that hinders corrosion.

3.4 Atomic force microscopy (AFM)

AFM is an approach utilized for morphological analysis of corroded surfaces at the micro to nanoscale, as it provides values of root-mean-square roughness (S_q), peak height (S_p) and average roughness (S_a).[46,47] Fig. 7 shows AFM images obtained after immersion of the mild steel coupons in different test environments.

As expected, the image for the blank (uninhibited $Ca(OH)_2$) system revealed rough surface morphology due to extensive and unrestrained corrosion damage. The surface roughness, S_q, and S_a, decreased remarkably with addition of the corrosion inhibitors (*C. albidum* and *C. afer* extracts), confirming their remarkable anticorrosion effects. This reduction in surface roughness supports the formation of a protective adsorbed layer. The changes are consistent with other bio-inhibitor studies, including those using *Ceramium rubrum*.[47]

© 2026 The Author(s). Published by the Royal Society of Chemistry

Open Access Article. Published on 20 November 2025. Downloaded on 6/21/2026 4:23:16 PM.
This article is licensed under a Creative Commons Attribution-NonCommercial 3.0 Unported Licence.

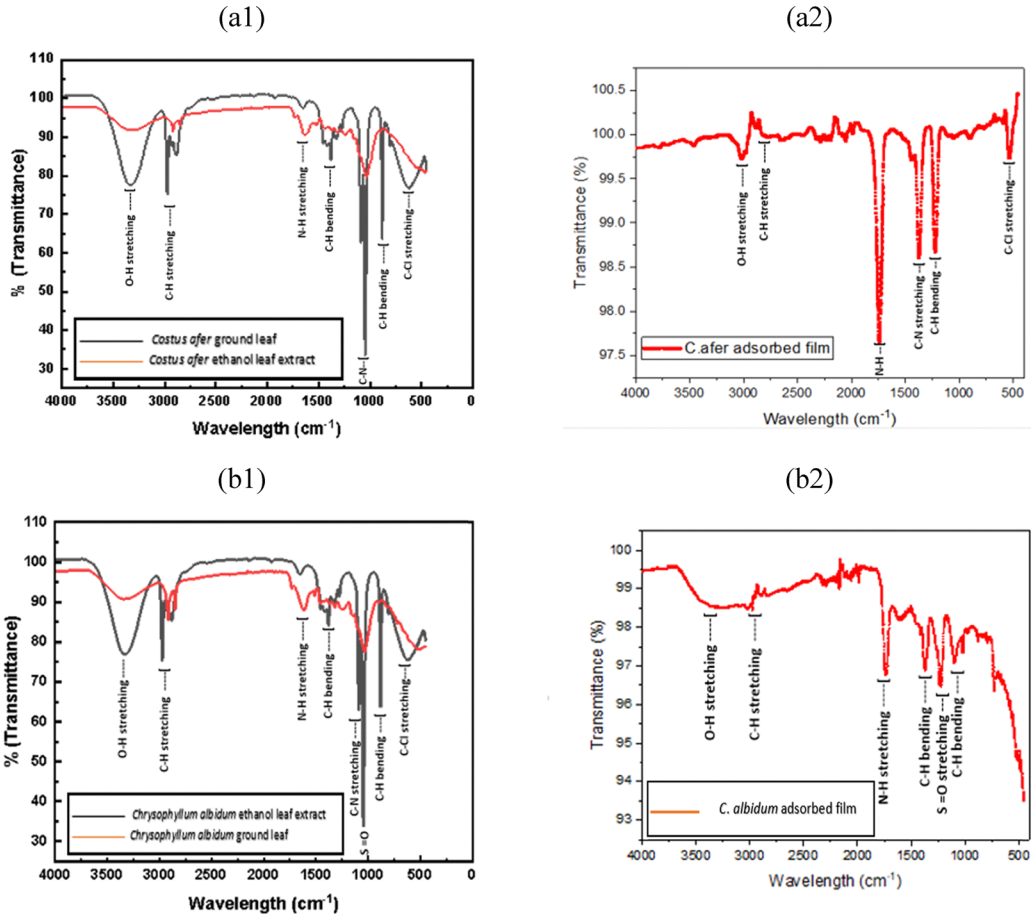

Fig. 6 FTIR spectra of the leaf powders and ethanol extract and corrosion products of (a1) (a2) *C. afer* and (b1) (b2) *C. albidum*.

Table 3 FTIR peak assignments and corresponding functional groups

Wavenumber (cm^{-1})	Functional group/bond	Class/compound type	Sample
3338.88/3339.01	O–H stretching	Alcohol (–OH)	*C. afer*, *C. albidum*
2974/2974.43	C–H stretching	Alkane	*C. afer*, *C. albidum*
2884/2884.62	C–H stretching	Alkane	*C. afer*, *C. albidum*
1654.23	N–H stretching	Amine salt	*C. albidum*
1380.39/1380.51	C–H bending	Aldehyde	*C. afer*, *C. albidum*
1328.32/1328.28	S═O stretching	Sulfone	*C. afer*, *C. albidum*
1087.68/1087.63	C–N stretching	Amine/imine/oxime	*C. afer*, *C. albidum*
1045.58	S═O stretching	Sulfoxide	*C. afer*
879.94/879.87	C–H bending	1,3-Disubstituted benzene	*C. afer*, *C. albidum*
619.92/611.43	C–Cl stretching	Halo compound	*C. afer*, *C. albidum*

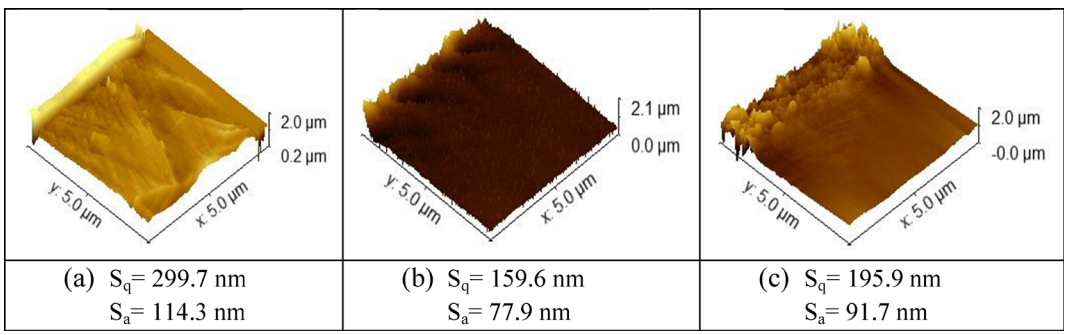

(a) S_q= 299.7 nm, S_a= 114.3 nm (b) S_q= 159.6 nm, S_a= 77.9 nm (c) S_q= 195.9 nm, S_a= 91.7 nm

Fig. 7 3D AFM topographic view of the coupons immersed in (a) uninhibited $Ca(OH)_2$, (b) $Ca(OH)_2$ with 0.5 g L^{-1} of *C. albidum* ethanol extract and (c) $Ca(OH)_2$ with 0.5 g L^{-1} of *C. afer* ethanol extract.

Open Access Article. Published on 20 November 2025. Downloaded on 6/21/2026 4:23:16 PM. This article is licensed under a Creative Commons Attribution-NonCommercial 3.0 Unported Licence.

3.5 Remote sensing assessment of fungal risk in urban concrete environments

The risk of fungal deterioration and corrosion of concrete in Port Harcourt and Owerri can be assessed by examining key environmental and industrial factors that contribute to such degradation. Both cities experience humid, high-rainfall climates that promote fungal growth and compromise concrete durability. Remote sensing analysis using 2025 Landsat 8 imagery was conducted to assess environmental susceptibility to fungal biodeterioration in two urban centres: Port Harcourt and Owerri, *via* the normalized difference moisture index (NDMI) and land use/land cover (LULC) mapping. NDMI results (Fig. 8) show that Port Harcourt had predominantly low values (−0.9255 to −0.38), indicating reduced vegetation moisture, while Owerri exhibited higher NDMI values (−0.7358 to −0.0035), reflecting more vegetated, moisture-retentive conditions.

Land use/land cover (LULC) analysis (Fig. 9) provided valuable environmental context. Port Harcourt exhibited a significantly higher proportion of paved surfaces (60.75%) compared to Owerri (36.71%), confirming its denser urban footprint. Impervious surfaces such as roads, buildings, and industrial areas are known to support fungal colonization in warm, humid climates. These surfaces retain moisture at the microscale, creating localized conditions conducive to fungal growth even in regions with low vegetation moisture. The elevated fungal risk in Port Harcourt is further linked to its intense industrialization, particularly oil and gas operations, which introduce additional environmental stressors, including acidic emissions, saline soils, and pollutant deposition. In contrast, Owerri's lower industrial activity and less severe urban stress result in a comparatively lower environmental risk, despite sharing similar macroclimatic conditions.

Although NDMI does not directly quantify surface moisture on concrete substrates, it offers useful insight into the broader microclimate. Port Harcourt, despite exhibiting lower NDMI values, was assigned a higher fungal deterioration risk score (3), driven by its high rainfall, humidity, and urban density. Owerri, with higher NDMI values and greater vegetative cover, received a moderate risk score (2). Taken together, the NDMI and LULC assessments informed a fungal deterioration risk factor scoring framework, summarized in Table 4.

3.6 Fungal identification and characterization

A total of seven fungal isolates were obtained from deteriorated concrete samples from Port Harcourt (Ozuoba) and Owerri (FUTO). Identified strains included *Aspergillus oryzae*, *A. niger*, *A. fumigatus*, *A. terreus*, and *Penicillium* spp. Morphological features and microscopic examination with lactophenol cotton

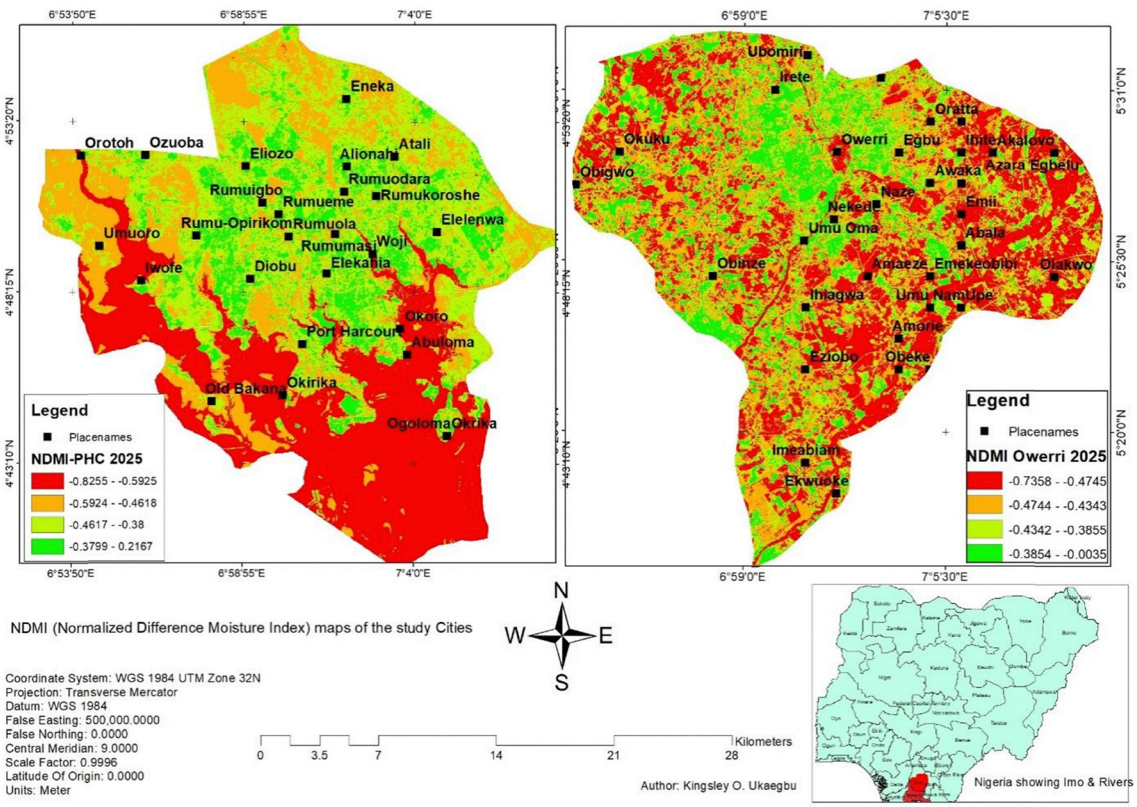

Fig. 8 Normalized difference moisture index (NDMI) maps of Port Harcourt (left) and Owerri (right) for 2025, derived from Landsat 8 imagery. The maps illustrate spatial variability in vegetation moisture, with red zones indicating drier, less vegetated areas and green zones representing higher moisture content. Port Harcourt shows more extensive low-NDMI regions, correlating with higher fungal deterioration risk due to increased surface exposure, impervious urban cover, and environmental stressors.

© 2026 The Author(s). Published by the Royal Society of Chemistry

Open Access Article. Published on 20 November 2025. Downloaded on 6/21/2026 4:23:16 PM. This article is licensed under a Creative Commons Attribution-NonCommercial 3.0 Unported Licence.

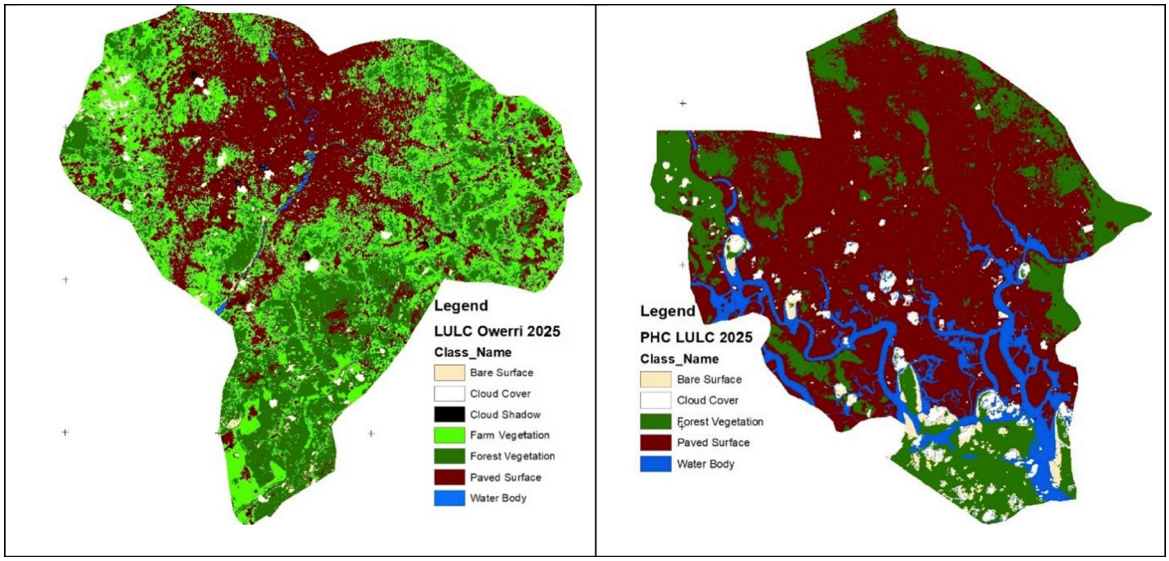

Fig. 9 Land use/land cover (LULC) classification map of Port Harcourt (left) and Owerri (right) for 2025, highlighting extensive areas of paved surfaces (red) and water bodies (blue), with limited vegetation cover. The dominance of impervious surfaces and fragmented green zones is indicative of dense urbanization and industrial development, factors that contribute to higher fungal biodeterioration risk by promoting surface exposure, reduced moisture retention, and pollutant accumulation.

blue stain confirmed identification. The fungal species observed in these samples are listed in Table 5, with respect to their isolate codes and their cultural and microscopic characteristics (Table 6).

Fungal species isolated from Ozuoba, Port Harcourt, included *Aspergillus terreus*, *Penicillium roqueforti*, and *Aspergillus fumigatus*, all known for their aggressive biodeteriorative potential. This combination places Ozuoba at a very high risk for fungal-induced concrete degradation (Fig. 8). In comparison, FUTO, Owerri, had a slightly more diverse but somewhat milder fungal profile, with the presence of *Aspergillus oryzae*, *Penicillium* spp., *A. terreus*, and the highly corrosive *A. niger*. While the overall fungal mix is less aggressive than that of Ozuoba, the inclusion of key degraders still results in a moderate to high risk designation for FUTO.

3.7 Antifungal susceptibility test

The antifungal activity of ethanol leaf extracts from *Costus afer* and *Chrysophyllum albidum* was evaluated using the agar well diffusion method against fungal strains isolated from FUTO (Owerri) and Ozuoba (Port Harcourt). Four concentrations were tested (12.5, 25, 50, and 100 mg mL^{-1}), with incubation at 26 °C for 24–48 hours. The diameters of the inhibition zones (mm) were measured and are summarized in Table 7.

The antifungal activity varied with both concentration and fungal strain. *C. albidum* demonstrated greater overall efficacy, with inhibition zones reaching up to 36 mm against *A. niger* (FUTO isolate). In contrast, *A. terreus* (PHC 1) exhibited complete resistance to both extracts. These results indicate strain-specific sensitivity, likely influenced by environmental adaptation. Comparatively, Iyabo *et al.*[48] reported inhibition zones of 14–22 mm for *A. niger* using similar plant extracts, whereas the present study achieved up to 36 mm, underscoring the superior antifungal potency of *C. albidum*.

Although both extracts exhibited measurable antifungal potential, the ethanol extract of *C. albidum* was significantly more effective (Fig. 10). This enhanced activity can be attributed to its broader range of bioactive constituents acting individually or synergistically. GC–MS analysis identified eight antifungal compounds in *C. afer*, including neophytadiene, squalene, 1-methyltetraisosane, α-tocospiro B and O, ethyl iso-allocholate, (*R*)-6*b*,8*a*-epoxy-octamethyl decahydro derivatives, and larossic acid acetate. While solvent effects were not explicitly examined, the use of a common solvent for both plant materials ensured that the observed differences in antifungal

Table 4 Risk factors and risk assessment for fungal deterioration and corrosion of concrete

	Scores			Risk assessment	
Factor	Low (1)	Medium (2)	High (3)	Port Harcourt	Owerri
Rainfall/humidity	<1500 mm per year	1500–2500 mm per year	>2500 mm per year	High	High
Temperature	<26 °C	26–28 °C	>28 °C	High	High
Industrial activity	Rural/remote	Semi-industrial	Oil/gas hubs	High	Low
Soil salinity/pH	pH 7–8, low salt	pH 6–7 or 8–9, moderate	pH <6 or >9, high salt	High	Moderate
Urbanization	Low population	Medium	High population density	High	Moderate

Open Access Article. Published on 20 November 2025. Downloaded on 6/21/2026 4:23:16 PM. This article is licensed under a Creative Commons Attribution-NonCommercial 3.0 Unported Licence.

Table 5 Identified fungal species and their cultural and microscopic characteristics

Isolate code/ location	Cultural characteristics of the SDA medium	Microscopic/morphological pattern	Identified species
PHC 1	Brown sporing/granular surface and yellow cracked reverse	Vesicles are hemispherical and phialides are produced from a primary row of Metula	*Aspergillus terreus*
PHC 2	Blue-green velvet surface and light reverse	Septate is profuse with branching, and conidiophores are long and branched with structures. Conidia are produced in dry chains from the tips of the phialides	*Penicillium roqueforti*
PHC 3	Smoked grey-green sporing/granular surface and light-yellow cracked reverse	Vesicles are globose and phialides are produced directly from the Metula	*Aspergillus fumigatus*
OWR 1	Yellowish green sporing/granular surface and light cracked reverse	Vesicles are globose and phialides are produced directly from the Metula	*Aspergillus oryzae*
OWR 2	Black sporing/granular surface and yellow cracked reverse	Septate hyphae with long conidiophores that support spherical vesicles that give rise to large Metula from which long chains of conidia are produced	*Aspergillus niger*
OWR 3	Brown sporing/granular surface and yellow cracked reverse	Vesicles are hemispherical and phialides are produced from a primary row of Metula	*Aspergillus terreus*
OWR 4	Blue velvet with white edge colony, reverse light yellow	Hyphae are hyaline and septate and produce brush-like conidiophores	*Penicillium* sp.

Table 6 Identified fungi (mould) species and their deterioration potential

Isolate code/location	Identified species	Known impact on concrete
PHC 1	*Aspergillus terreus*	Acid-producing, moderate concrete degrader
PHC 2	*Penicillium roqueforti*	Known biodeteriorant, secretes organic acids
PHC 3	*Aspergillus fumigatus*	Thermotolerant, known for biofilm formation
OWR 1	*Aspergillus oryzae*	Mildly invasive, low direct impact
OWR 2	*Aspergillus niger*	High acid producer (oxalic, citric) → corrosive
OWR 3	*Aspergillus terreus*	Acid-producing, moderate concrete degrader
OWR 4	*Penicillium* spp.	Varies, mostly moderate impact

Table 7 Antifungal activities of different concentrations of ethanolic leaf extracts of *C. afer* and *C. albidum* and the inhibition zone diameter

	Inhibition zone diameter (mm)			
Fungal strain	12.5 mg mL^{-1}	25 mg mL^{-1}	50 mg mL^{-1}	100 mg mL^{-1}
C. afer				
FUTO 1–*Aspergillus oryzae*	**0**	**0**	0	18
FUTO 2–*Aspergillus niger*	**0**	**0**	3	17
FUTO 3–*Aspergillus terreus*	**2**	**7**	18	28
FUTO 4–*Penicillium* spp.	**0**	**0**	5	15
PHC 1–*Aspergillus terreus*	**0**	**0**	0	0
PHC 2–*Penicillium roqueforti*	**0**	**4**	10	15
PHC 3–*Aspergillus fumigatus*	**0**	**0**	0	10
C. albidum				
FUTO 1–*Aspergillus oryzae*	0	2	15	24
FUTO 2–*Aspergillus niger*	25	36	18	28
FUTO 3–*Aspergillus terreus*	0	14	20	22
FUTO 4–*Penicillium* spp.	0	18	20	24
PHC 1–*Aspergillus terreus*	0	0	0	0
PHC 2–*Penicillium roqueforti*	0	2	18	20
PHC 3–*Aspergillus fumigatus*	0	0	0	20

activity primarily reflect intrinsic compositional variations rather than solvent bias.

In contrast, *C. albidum* yielded twelve active compounds, including squalene, cyclononasiloxane, cyclotetrasiloxane, alpha-tocopherol, fatty acid esters (hexadecanoic acid and octadecenoic acid), eicosane, neophytadiene, 3,7,11,15-tetramethyl-2-hexadecen-1-ol, lup-20(29)-en-3-ol acetate, 7,8-epoxylanostan-11-ol-3-one, and 9,19-cyclolanostan-3-ol acetate. Many of these compounds, such as squalene, tocopherols, and cyclotetrasiloxanes, are known to exert membrane-disruptive and oxidative stress-inducing effects in fungal cells.

The superior antifungal activity of *C. albidum* aligns with findings from previous studies. For example, squalene, alpha-tocopherol, neophytadiene, and fatty acid esters have been reported to possess significant antifungal or antimicrobial activity.[49,50] In contrast, *C. afer* has shown more species-specific antifungal activity, with Sonibare *et al.*[51] noting variable efficacy depending on fungal type and concentration. The smaller number of active antifungal constituents in *C. afer* observed in this study supports this limited-spectrum behavior.

Fungal isolates from Port Harcourt and Owerri exhibited distinct susceptibility patterns, aligning with environmental observations from each location. In Port Harcourt, *Aspergillus terreus* remained resistant to all concentrations of both *Costus afer* and *Chrysophyllum albidum* extracts. This resistance is likely linked to long-term adaptation to harsh environmental stressors such as hydrocarbon pollutants, salinity, and industrial emissions, consistent with earlier findings on microbial resilience in the region.[52–54] Other fungal strains from Port Harcourt (*e.g.*, *P. roqueforti* and *A. fumigatus*) were effectively inhibited, particularly by *C. albidum*, suggesting selective vulnerability despite the area's classification as a very high-risk site. These findings support previous reports on the antifungal action of bioactive compounds such as squalene and tocopherol in biomass extracts.[30,31] With consistent application, the biological threat level at Port Harcourt could potentially be downgraded from "very high" to "moderate to high." In

© 2026 The Author(s). Published by the Royal Society of Chemistry

Open Access Article. Published on 20 November 2025. Downloaded on 6/21/2026 4:23:16 PM.
This article is licensed under a Creative Commons Attribution-NonCommercial 3.0 Unported Licence.

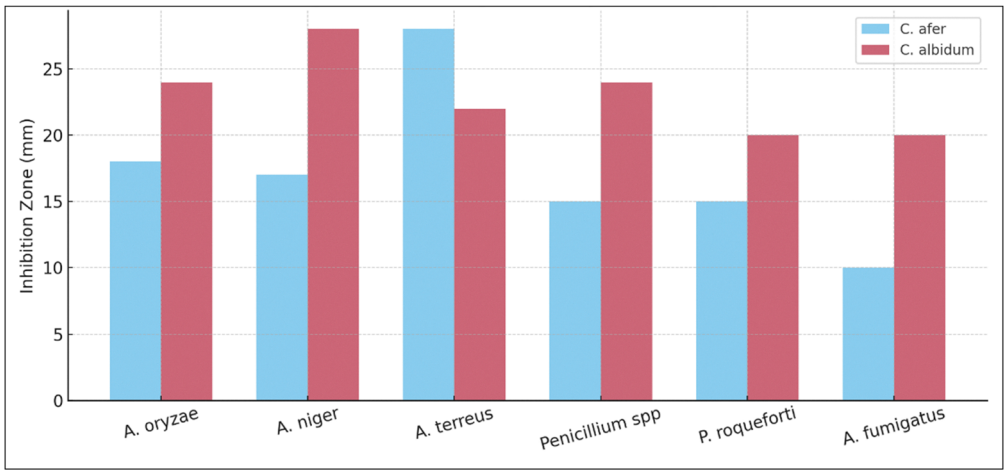

Fig. 10 Antifungal activity of 100 mg mL^{-1} ethanol extracts of *C. afer* and *C. albidum* leaves.

contrast, fungal isolates from Owerri, including *A. oryzae*, *A. niger*, *A. terreus*, and *Penicillium* spp., demonstrated mixed but generally higher susceptibility to both extracts. *A. niger*, a well-known concrete-degrading species, was strongly inhibited by *C. albidum*, corroborating earlier reports of its efficacy.[8,55] Although *A. terreus* showed resistance in both locations, the broad-spectrum activity of *C. albidum* against multiple strains underscores its potential as a viable antifungal agent for humid environments such as Owerri.

These biological trends correspond well with spatial environmental indicators. Port Harcourt's low NDMI values and high proportion of impervious surfaces reflect a harsher urban microclimate conducive to fungal persistence and resistance. Meanwhile, Owerri's higher NDMI and vegetative cover correlate with lower fungal resistance and reduced risk. These findings highlight the complex interplay between vegetation moisture, land use, and microbial adaptation. While NDMI provides a useful regional overview, this study affirms the importance of integrating local-scale microbial diagnostics with remote sensing tools for accurate fungal risk mapping and development of site-specific bioprotection strategies.

4. Conclusion

This study confirms the significant potential of *Costus afer* and *Chrysophyllum albidum* ethanol leaf extracts as dual-function, bio-based additives for enhancing the durability of reinforced concrete. Both extracts demonstrated substantial antifungal and anticorrosion activity, with *C. albidum* consistently outperforming across most metrics. These findings align with recent advances in self-healing and eco-sustainable concrete technologies employing plant-derived modifiers.

Phytochemical characterization using GC–MS and FTIR confirmed the presence of bioactive compounds such as flavonoids, alkaloids, and siloxanes, known for their antimicrobial and corrosion-inhibiting properties. Electrochemical analysis revealed significant reductions in corrosion current density and notable increases in charge transfer resistance, with *C. albidum* achieving inhibition efficiencies as high as 99.8%. These electrochemical trends were validated by AFM surface morphology, which showed reduced roughness and evidence of protective film formation. Antifungal assays further demonstrated strong inhibitory effects against concrete-degrading fungi, including *Aspergillus niger*, *A. terreus*, and *Penicillium* spp.

In comparison with conventional synthetic and natural inhibitors reported in the literature, these biomass-based treatments offer competitive or superior performance while remaining non-toxic, biodegradable, cost-effective, and locally sourced. Their integration into concrete coatings, admixtures, or steel reinforcement protection systems represents a promising strategy for sustainable infrastructure, especially in tropical, marine, or industrial regions susceptible to microbial degradation and chloride-induced corrosion.

Notably, this work also highlights the utility of remote sensing tools such as NDMI and LULC mapping as valuable complements to laboratory diagnostics. These tools offer spatial insight into environmental moisture and land cover dynamics that influence fungal colonization potential in urban concrete environments.

Future work should prioritize long-term field validation of the extracts under real-world exposure conditions, assessment of synergistic effects through multi-extract or nanoadditive formulations, and compatibility studies with conventional concrete admixtures. Additionally, expanded remote sensing applications incorporating indices such as NDVI or land surface temperature (LST) and microclimate modelling could enhance the predictive accuracy of fungal risk assessments. Finally, investigating the response of biofilm-forming fungal consortia to these extracts will help establish their robustness against complex microbial communities commonly found in deteriorating infrastructures.

Conflicts of interest

The authors declare that no competing interests exist.

Open Access Article. Published on 20 November 2025. Downloaded on 6/21/2026 4:23:16 PM. This article is licensed under a Creative Commons Attribution-NonCommercial 3.0 Unported Licence.

Data availability

The datasets generated and/or analyzed during the current study are available from the corresponding authors on reasonable request. The data will be stored in a secure data repository and will be made accessible to the public upon publication. The data will be formatted according to community standards to facilitate reuse and analysis.

The data supporting this article have been included as part of the supplementary information (SI). Supplementary information: experimental data on antifungal and corrosion-inhibiting properties of Costus afer and Chrysophyllum albidum extracts; material characterization data (*e.g.*, FTIR, GC-MS, electrochemical impedance spectroscopy, potentiodynamic polarisation); antifungal susceptibility test results; remote sensing. See DOI: https://doi.org/10.1039/d5ma00687b.

Acknowledgements

The authors sincerely appreciate the financial support provided by the World Bank and the French Development Agency through the Second Africa Higher Education Centres of Excellence for Development Impact (ACE Impact) Project – P169064, IDA No. 6510-NG.

References

1 J. Biswas, K. Sharma, K. K. Harris and Y. Rajput, Biodeterioration agents: Bacterial and fungal diversity dwelling in or on the pre-historic rock-paints of Kabra-pahad, India, *Iran. J. Microbiol.*, 2013, **5**(3), 309–314.

2 J. A. Maresca, P. Moser and T. Schumacher, Analysis of bacterial communities in and on concrete, *Mater. Struct.*, 2016, **50**(1), 25.

3 H. Yang, W. Li, X. Liu, A. Liu, P. Hang and R. Ding, *et al.*, Preparation of corrosion inhibitor loaded zeolites and corrosion resistance of carbon steel in simulated concrete pore solution, *Constr. Build. Mater.*, 2019, **225**, 90–98, DOI: 10.1016/j.conbuildmat.2019.07.141.

4 S. Bhattacharyya, S. Akhtar, A. Chaudhuri, S. Mahanty, P. Chaudhuri and M. Sudarshan, Affirmative nanosilica mediated approach against fungal biodeterioration of concrete materials, *Case Stud. Constr. Mater.*, 2022, **17**, e01258, DOI: 10.1016/j.cscm.2022.e01258.

5 A. Bertron, Understanding interactions between cementitious materials and microorganisms: a key to sustainable and safe concrete structures in various contexts, *Mater. Struct.*, 2014, **47**(11), 1787–1806.

6 R. P. George, S. Ramya, D. Ramachandran and U. Kamachi Mudali, Studies on Biodegradation of normal concrete surfaces by fungus *Fusarium* sp, *Cem. Concr. Res.*, 2013, **47**, 8–13, DOI: 10.1016/j.cemconres.2013.01.010.

7 M. Ljaljevic-Grbic and J. Vukojevic, Role of fungi in biodeterioration process of stone in historic buildings, *Zb. Matice Srp. Prir. Nauke*, 2009, **116**, 245–251.

8 L. Jiang, T. R. Pettitt, N. Buenfeld and S. R. Smith, A critical review of the physiological, ecological, physical and chemical factors influencing the microbial degradation of concrete by fungi, *Building and Environment*, Pergamon, 2022, vol. 214, p. 108925.

9 A. Chaudhuri, S. Bhattacharyya, P. Chaudhuri, M. Sudarshan and S. Mukherjee, In vitro deterioration study of concrete and marble by *Aspergillus tamarii*, *J. Build. Eng.*, 2020, **32**, 101774, DOI: 10.1016/j.jobe.2020.101774.

10 J. Blunt, G. Jen and C. P. Ostertag, Enhancing corrosion resistance of reinforced concrete structures with hybrid fiber reinforced concrete, *Corros. Sci.*, 2015, **92**, 182–191.

11 R. Liu, L. Jiang, J. Xu, C. Xiong and Z. Song, Influence of carbonation on chloride-induced reinforcement corrosion in simulated concrete pore solutions, *Constr. Build. Mater.*, 2014, **56**, 16–20, DOI: 10.1016/j.conbuildmat.2014.01.030.

12 M. H. Sliem, A. B. Radwan, F. S. Mohamed, N. A. Alnuaimi and A. M. Abdullah, An efficient green ionic liquid for the corrosion inhibition of reinforcement steel in neutral and alkaline highly saline simulated concrete pore solutions, *Sci. Rep.*, 2020, **10**(1), 1–15, DOI: 10.1038/s41598-020-71222-4.

13 M. Liu, X. Cheng, X. Li, Z. Jin and H. Liu, Corrosion behavior of Cr modified HRB400 steel rebar in simulated concrete pore solution, *Constr. Build. Mater.*, 2015, **93**, 884–890, DOI: 10.1016/j.conbuildmat.2015.05.073.

14 W. Wang, H. Chen, X. Li and Z. Zhu, Corrosion behavior of steel bars immersed in simulated pore solutions of alkali-activated slag mortar, *Constr. Build. Mater.*, 2017, **143**, 289–297, DOI: 10.1016/j.conbuildmat.2017.03.132.

15 I. I. N. Etim, J. Dong, J. Wei, C. Nan, E. Felix Daniel and D. Babu Subedi, *et al.*, Mitigation of sulphate-reducing bacteria attack on the corrosion of 20SiMn steel rebar in sulphoaluminate concrete using organic silicon quaternary ammonium salt, *Constr. Build. Mater.*, 2020, **257**, 119047, DOI: 10.1016/j.conbuildmat.2020.119047.

16 X. Feng, Y. Zuo, Y. Tang, X. Zhao and J. Zhao, The influence of strain on the passive behavior of carbon steel in cement extract, *Corros. Sci.*, 2012, **65**, 542–548, DOI: 10.1016/j.corsci.2012.08.060.

17 A. A. Adewumi, M. Maslehuddin, S. U. Al-Dulaijan and M. Shameem, Corrosion behaviour of carbon steel and corrosion resistant steel under elevated temperature and chloride concentration in simulated concrete pore solution, *Eur. J. Environ. Civ. Eng.*, 2021, **25**(3), 452–467, DOI: 10.1080/19648189.2018.1531270.

18 F. Liu, L. Zhang, X. Yan, X. Lu, Y. Gao and C. Zhao, Effect of diesel on corrosion inhibitors and application of bio-enzyme corrosion inhibitors in the laboratory cooling water system, *Corros. Sci.*, 2015, DOI: 10.1016/j.corsci.2015.01.028.

19 A. Poursaee, Corrosion of steel bars in saturated Ca(OH)2 and concrete pore solution, *Concr. Res. Lett.*, 2010, **1**(3), 90–97. Available from: https://www.issres.net/journal/index.php/crl/article/view/106.

20 B. Li, K. Huang, S. Xue, W. Liu and J. Li, Robust Slippery Liquid-Infused Porous Surfaces with Fast Self-Replenishment Properties for Anticontaminant, Anti-Icing, and Anticorrosion

© 2026 The Author(s). Published by the Royal Society of Chemistry

Open Access Article. Published on 20 November 2025. Downloaded on 6/21/2026 4:23:16 PM. This article is licensed under a Creative Commons Attribution-NonCommercial 3.0 Unported Licence.

Applications on Magnesium Alloys, *ACS Appl. Mater. Interfaces*, 2025, **17**(12), 19105–19116. Available from: https://pubs.acs.org/doi/abs/10.1021/acsami.4c23018.

21 R. Bhola, S. M. Bhola, B. Mishra and D. L. Olson, Microbiologically influenced corrosion and its mitigation: (A review), *Mater. Sci. Res. India*, 2010, **7**(2), 407–412.

22 J. Wang, H. Liu, Y. Gao, Q. Yue, B. Gao and B. Liu, *et al.*, Pilot-scale advanced treatment of actual high-salt textile wastewater by a UV/O3 pressurization process: Evaluation of removal kinetics and reverse osmosis desalination process, *Sci. Total Environ.*, 2023, **857**, 159725. Available from: https://www.sciencedirect.com/science/article/abs/pii/S0048969722068255.

23 L. Kong, J. Fang, X. Zhou, M. Han and H. Lu, Assessment of coatings for protection of cement paste against microbial induced deterioration through image analysis, *Constr. Build. Mater.*, 2018, **191**, 342–353, DOI: 10.1016/j.conbuildmat.2018.10.041.

24 I. I. N. Etim, J. Dong, J. Wei, C. Nan, D. B. Pokharel and A. J. Umoh, *et al.*, Effect of organic silicon quaternary ammonium salts on mitigating corrosion of reinforced steel induced by SRB in mild alkaline simulated concrete pore solution, *J. Mater. Sci. Technol.*, 2021, **64**, 126–140.

25 W. Yan, S. Xue, X. Zhao, W. Zhang and J. Li, Hexagonal boron nitride based slippery liquid infused porous surface with anti-corrosion, anti-contaminant and anti-icing properties for protecting magnesium alloy, *Chin. Chem. Lett.*, 2024, **35**(4), 109224. Available from: https://www.sciencedirect.com/science/article/abs/pii/S1001841723009750.

26 B. N. AL-Kharabsheh, M. M. Arbili, A. Majdi, S. M. Alogla, A. Hakamy and J. Ahmad, *et al.*, Basalt Fibers Reinforced Concrete: Strength and Failure Modes, *Mater*, 2022, **15**(20), 7350. Available from: https://www.mdpi.com/1996-1944/15/20/7350/htm.

27 B. U. Maheswari and G. Kalaiselvi, Exploring Neophytadiene from Ampelocissus araneosa: A Molecular Docking Approach to Inhibit Biofilm Formation in Staphylococcus aureus, *Uttar Pradesh J. Zool.*, 2024, **45**(3), 59–70.

28 M. Chhillar and M. A. Khan, Therapeutic prospects of neophytadiene from datura stramonium: a potential bioactive compound for medicinal interventions, *Asian J. Pharm. Clin. Res.*, 2025, **18**(4), 112–119. Available from: https://www.scribd.com/document/932039756/AJPCR-54111-20250408-V3.

29 J. Song, N. Shang, N. Baig, J. Yao, C. Shin and B. K. Kim, *et al.*, Aspergillus flavus squalene synthase as an antifungal target: Expression, activity, and inhibition, *Biochem. Biophys. Res. Commun.*, 2019, **512**(3), 517–523.

30 M. Micera, A. Botto, F. Geddo, S. Antoniotti, C. M. Bertea and R. Levi, *et al.*, Squalene: More than a Step toward Sterols, *Antioxidants*, 2020, **9**(8), 1–14. Available from: https://pubmed.ncbi.nlm.nih.gov/32748847/.

31 D. Keshari, A. D. Tripathi, A. Agarwal, S. Rai, S. K. Srivastava and P. Kumar, Effect of α-dl tocopherol acetate (antioxidant) enriched edible coating on the physicochemical, functional properties and shelf life of minimally processed carrots (Daucus carota subsp. sativus), *Future Foods*, 2022, **5**, 100116. Available from: https://www.sciencedirect.com/science/article/pii/S2666833522000041.

32 C. Jianu, L. C. Rusu, I. Muntean, I. Cocan, A. T. Lukinich-Gruia and I. Goleț, *et al.*, In Vitro and In Silico Evaluation of the Antimicrobial and Antioxidant Potential of Thymus pulegioides Essential Oil, *Antioxidants*, 2022, **11**(12), 2472. Available from: https://www.mdpi.com/2076-3921/11/12/2472/htm.

33 J. A. Prieto-Rodríguez, K. P. Lévuok-Mena, J. C. Cardozo-Muñoz, J. E. Parra-Amin, F. Lopez-Vallejo and L. E. Cuca-Suárez, *et al.*, In Vitro and In Silico Study of the α-Glucosidase and Lipase Inhibitory Activities of Chemical Constituents from Piper cumanense (Piperaceae) and Synthetic Analogs, *Plants*, 2022, **11**(17), 2188. Available from: https://www.mdpi.com/2223-7747/11/17/2188/htm.

34 O. A. Pratama, W. A. S. Tunjung, S. Sutikno and B. S. Daryono, Bioactive compound profile of melon leaf extract (Cucumis melo l. 'Hikapel') infected by downy mildew, *Biodiversitas*, 2019, **20**(11), 3448–3453.

35 M. P. Bhat, R. S. Kumar, B. Chakraborty, S. K. Nagaraja, K. Gireesh Babu and S. Nayaka, Eicosane: An antifungal compound derived from Streptomyces sp. KF15 exhibits inhibitory potential against major phytopathogenic fungi of crops, *Environ. Res.*, 2024, **251**, 118666.

36 E. E. Oguzie, Corrosion Inhibitive Effect and Adsorption Behaviour of Hibiscus Sabdariffa Extract on Mild Steel in Acidic Media, *Port. Electrochim. Acta*, 2008, **26**(3), 303–314.

37 E. E. Oguzie, Adsorption and corrosion inhibitive properties of Azadirachta indica in acid solutions, *Pigm. Resin Technol.*, 2006, **35**(6), 334–340, DOI: 10.1108/03699420610711335.

38 E. E. Oguzie, C. E. Ogukwe, J. N. Ogbulie, F. C. Nwanebu, C. B. Adindu and I. O. Udeze, *et al.*, Broad spectrum corrosion inhibition: Corrosion and microbial (SRB) growth inhibiting effects of Piper guineense extract, *J. Mater. Sci.*, 2012, **47**(8), 3592–3601.

39 I. V. Onuegbu, O. E. Emmanuel and A. S. Aguguom, Electrochemical, Sem, Gc-Ms and ftir study of inhibitory property of cold extract of theobroma cacao pods for mild steel corrosion in hydrochloric acid, *Int. J. Eng. Trends Technol.*, 2020, **68**(2), 82–87.

40 Z. Zhang, H. Ba and Z. Wu, Sustainable corrosion inhibitor for steel in simulated concrete pore solution by maize gluten meal extract: Electrochemical and adsorption behavior studies, *Constr. Build. Mater.*, 2019, **227**, 117080, DOI: 10.1016/j.conbuildmat.2019.117080.

41 Y. Meng, S. Li and Z. Zhang, Inhibition performance of uniconazole on steel corrosion in simulated concrete pore solution: An eco-friendly way for steel protection, *Heliyon*, 2024, **10**(3), e24688, DOI: 10.1016/j.heliyon.2024.e24688.

42 Y. Liu, Z. Song, W. Wang, L. Jiang, Y. Zhang and M. Guo, *et al.*, Effect of ginger extract as green inhibitor on chloride-induced corrosion of carbon steel in simulated concrete pore solutions, *J. Cleaner Prod.*, 2019, **214**, 298–307.

43 D. Liu, Y. Jian, Y. Tang, K. Cao, W. Zhang and H. Chen, *et al.*, Comprehensive Testing of Sulfate Erosion Damage of Concrete Structures and Analysis of Silane Coating Protection Effect, *Sensors*, 2022, **22**(20), 7991.

44 Y. Zhang, D. Lou, P. Tan and Z. Hu, Experimental study on the emission characteristics of a non-road diesel engine

Open Access Article. Published on 20 November 2025. Downloaded on 6/21/2026 4:23:16 PM. This article is licensed under a Creative Commons Attribution-NonCommercial 3.0 Unported Licence.

equipped with different after-treatment devices, *Environ. Sci. Pollut. Res.*, 2019, **26**(26), 26617–26627.

45 E. E. Elemike, O. E. Fayemi, A. C. Ekennia, D. C. Onwudiwe and E. E. Ebenso, Silver Nanoparticles Mediated by *Costus afer* Leaf Electrochemical Properties, *Molecules*, 2017, **22**(20), 7991.

46 C. P. Onuoha, I. N. Etim and E. E. Oguzie, Corrosion protection of mild steel in water-in-diesel emulsion using *Ocimum gratissimum* extract, *Vietnam J. Chem.*, 2024, 1–9.

47 A. Fouda, E. El-shereafy, A. A. Hathoot and N. M. El-bahrawi, Corrosion Inhibition of Aluminum by Cerumium rubrum Extract in Hydrochloric Acid Environment, *J. Bio- Tribo-Corrosion*, 2020, DOI: 10.1007/s40735-020-0330-9.

48 O. G. Iyabo, O. Z. Vianne, O. M. Ikhiwili and A. Bosede, In vitro antibacterial and antifungal activities of *Chrysophyllum albidum* and *Diospyros monbuttensis* leaves, *J Pharmacogn Phyther*, 2016, **8**(1), 1–7.

49 N. Ali Al-Mekhlafi, H. A. Golah, A. Mediani, M. Saad Al-Ezzi, W. S. M. Qadi and A. Sharyan, *et al.*, Phytochemical analysis and antifungal activity of selected medicinal plants extracts against Candida albicans, *World J. Pharm. Pharm. Sci.*, 2024, **13**(7). Available from: https://www.researchgate.net/publication/382793586_PHYTOCHEMICAL_ANALYSIS_AND_ANTIFUNGAL_ACTIVITY_OF_SELECTED_MEDICINAL_PLANTS_EXTRACTS_AGAINST_CANDIDA_ALBICANS.

50 S. Albayrak, A. Aksoy, O. Sagdic and E. Hamzaoglu, Compositions, antioxidant and antimicrobial activities of Helichrysum (Asteraceae) species collected from Turkey, *Food Chem.*, 2010, **119**(1), 114–122.

51 M. A. Sonibare, A. O. Isola and O. J. Akinmurele, Pharmacognostic standardisation of the leaves of *Costus afer* Ker Gawl. (Zingiberaceae) and Palisota hirsuta (Thunb.) K. Schum. (Commelinaceae), *Future J. Pharm. Sci.*, 2023, **9**(1), 1–16, DOI: 10.1186/s43094-023-00469-1.

52 C. C. Iheanacho, I. L. Nkwocha, T. Mgbede, M. A. Abah, A. S. Osagie and E. C. Nonye, *et al.*, Physicochemical and Fungal Analysis of a Hydrocarbon-Polluted Soil at Amadi-Ama Creek of Bonny River Port Harcourt, Rivers State, Nigeria, *Asian J. Sci. Technol. Eng. Art*, 2024, **2**(5), 664–676.

53 O. N. Akomah-Abadaike and E. A. Chumu, Antibiotics and Antifungal Resistance Patterns of Microbial Isolates from Dish Washing Sponges in the University of Port-Harcourt, Nigeria, *Asian J. Biol.*, 2023, **19**(1), 45–52. Available from: https://journalajob.com/index.php/AJOB/article/view/358.

54 A. M. Rabab, S. T. Asmaa, H. M. Asmaa and A. S. Shereen, Adaptability assessment of Aspergillus niger and Aspergillus terreus isolated from long-term municipal/industrial effluent-irrigated soils to cadmium stress, *BMC Microbiol.*, 2025, **25**(1), 297. Available from: https://bmcmicrobiol.biomedcentral.com/articles/10.1186/s12866-025-04000-9.

55 I. Khokhar, M. S. Haider, I. Mukhtar and S. Mushtaq, Biological control of Aspergillus niger, the cause of Black-rot disease of Allium cepa L. (onion), by Penicillium species, *J. Agrobiol.*, 2013, **29**(1), 23–28.

© 2026 The Author(s). Published by the Royal Society of Chemistry